Accelerated evolution of convective simulations

Evan H. Anders and Benjamin P. Brown

Dept. Astrophysical & Planetary Sciences, University of Colorado – Boulder, Boulder, CO 80309, USA and
Laboratory for Atmospheric and Space Physics, Boulder, CO 80303, USA

Jeffrey S. Oishi

Department of Physics and Astronomy, Bates College, Lewiston, ME 04240, USA

High Rayleigh number, turbulent convection is a classic system with a large timescale separation between flow speeds and equilibration time. In this paper, we present a method of achieving Accelerated Evolution (AE) of convective simulations which fast-forwards through the long thermal evolution of these systems, and we test the validity of this method. The AE procedure involves measuring the dynamics of convection early in a simulation and using its characteristics to adjust the mean thermodynamic profile within the domain towards its evolved state. We study Rayleigh-Bénard convection as a test case for AE. Evolved flow properties of AE solutions are measured to be within a few percent of solutions which are reached through standard evolution over a full thermal timescale. We conclude with a discussion of useful extensions of AE, including stratified, compressible convection or stellar structure models.

I. INTRODUCTION

Astrophysical convection occurs in the presence of disparate timescales. Studying realistic models of natural systems through direct numerical simulations is infeasible due to the large separation between various flow timescales and equilibration times. Stiffness in astrophysical systems can manifest in multiple ways, some of which can be handled by clever choices of numerical algorithms, and some which cannot. For example, flows in the convection zones of stars like the Sun are characteristically low Mach number (Ma) in the deep interior. Initial value problems solved using explicit timestepping methods are bound by the Courant-Friedrich-Lewy (CFL) timestep limit corresponding to the fastest motions (sound waves), resulting in timesteps which are prohibitively small for studies of the deep, low-Ma motions. These systems are numerically stiff, and the difference between the sound crossing time and the convective overturn time has made studies of low-Ma stellar convection difficult. This stiffness can be avoided using approximations such as the anelastic approximation, in which sound waves are explicitly filtered out [1, 2]. Recently, advanced numerical techniques which use fully implicit [3–5] or mixed implicit-explicit [6–8] timestepping mechanisms have made it possible to study convection in the fully compressible equations at low Mach numbers, and careful studies of deep convection which would have been impossible a decade ago are now widely accessible.

Unfortunately, convective systems are stiff in more than one timescale and generally evolve over the course of thermal timescales, which are often much larger than all relevant dynamical timescales. Transport by convection is a highly nonlinear process, and this makes addressing the stiffness much more challenging; even fully implicit methods remain bound by the nonlinear flow timescales [3–5]. Resolving dynamics in atmospheres which are sufficiently thermally relaxed remains a challenging problem. Solar convection is a prime example of this phenomenon, as dynamical timescales in the solar convective zone are relatively short (convection overturns every ~ 5 minutes at the solar surface) compared to the Sun's Kelvin-Helmholtz timescale of $3 \cdot 10^7$ years [9]. In such a system, it is impossible to resolve the convective dynamics while also meaningfully evolving the thermal structure of the system using traditional timestepping techniques alone. As modern simulations aim to model natural convection in the high-Rayleigh-number (Ra) regime, the thermal diffusion timescale (t_κ, defined in section III) becomes intractably large compared to dynamical timescales such as the freefall time ($t_{\rm ff}$, defined in section II) [7],

$$\frac{t_\kappa}{t_{\rm ff}} \propto ({\rm Ra})^{1/2}. \tag{1}$$

Furthermore, as dynamical and thermal timescales separate, simulations become more turbulent. Capturing appropriately resolved turbulent motions requires finer grid meshes and smaller timesteps. Thus, the progression of simulations into the high-Ra regime of natural convection is slowed by two simultaneous effects: timestepping through a single convective overturn time becomes more computationally expensive and the number of overturn times required for systems to reach thermal equilibration grows.

The vast difference between convective and thermal timescales has long plagued numericists studying convection, and an abundance of approaches has been employed to study thermally converged solutions. One popular method for accelerating the convergence of high-Ra solutions is by "bootstrapping" – the process of using the flow fields in a converged solution at low Ra as initial conditions for a simulation at high Ra. This method has been used with

great success [10, 11], but it is not without its faults. Bootstrapped solutions are susceptible to hysteresis effects, in which large-scale convective structures present in the low Ra solution imprint onto the dynamics of the new, high Ra solution. Another commonly-used tactic in moderate-Ra simulations is to first solve a simple model of the system in question, and then use the solution of that model as initial conditions for full nonlinear direct numerical simulations. For example, past studies have used initial conditions from a linear eigenvalue solve [12] in plane-parallel studies, or axisymmetric solutions in studies of convection in 3D cylinders [11]. In other systems, particularly when convective zones are adjacent to stable regions, authors often choose initial conditions which are not in a classic, hydrostatic, conductive state. Rather, either through knowledge of low-Ra solutions [13] or broader convective theories such as Mixing Length Theory [14], initial conditions can be adjusted such that the stratification within the convective domain is closer to an equilibrium state than the largely unstable hydrostatic state.

Despite the numerous methods that have been used, the most straightforward way to achieve a thermally converged solution is to evolve a convective simulation through a thermal timescale. Some modern studies do just that [2]. Such evolution is computationally *expensive*, and state-of-the-art simulations at the highest values of Ra can only reasonably be run for hundreds of freefall timescales [15], much less the thousands or millions of freefall times required for thermal convergence.

In this work, we study a method of achieving accelerated evolution of convective simulations. We couple measurements of the dynamics of unequilibrated convective simulations with knowledge about energy balances in the desired solution to self-consistently adjust the mean vertical thermodynamic profile towards its evolved state. While a technique of this kind has been used previously [16], the details of implementation, the convergence properties, and whether or not the accelerated evolution state corresponds to a standard evolution state are not documented. In section II, we describe our convective simulations and numerical methods. In section III, we describe the procedure for achieving accelerated evolution. In section IV, we compare accelerated evolution solutions to solutions obtained from standard evolution through a full thermal diffusion timescale. Finally, in section V, we offer concluding remarks and discuss extensions of the methods presented here.

II. EXPERIMENT

In this work we study a simple form of thermal convection: incompressible Rayleigh-Bénard convection under the Oberbeck-Boussinesq approximation, such that the fluid has a constant kinematic viscosity (ν), thermal diffusivity (κ), and coefficient of thermal expansion (α). The density of the fluid is a constant, ρ_0, except in the buoyancy term, where it is $\rho = \rho_0(1 - \alpha T_1)$. The gravitational acceleration, $\boldsymbol{g} = -g\hat{\boldsymbol{z}}$, is constant. The equations of motion are [17]:

$$\nabla \cdot \boldsymbol{u} = 0, \tag{2}$$

$$\frac{\partial \boldsymbol{u}}{\partial t} + \boldsymbol{u} \cdot \nabla \boldsymbol{u} = -\frac{1}{\rho_0}\nabla P - g(1 - \alpha T_1)\hat{z} + \nu\nabla^2 \boldsymbol{u}, \tag{3}$$

$$\frac{\partial T_1}{\partial t} + \boldsymbol{u} \cdot \nabla(T_0 + T_1) = \kappa\nabla^2 T_1, \tag{4}$$

where $\boldsymbol{u} = u\hat{\boldsymbol{x}} + v\hat{\boldsymbol{y}} + w\hat{\boldsymbol{z}}$ is the velocity, $T = T_0(z) + T_1(x, y, z, t)$ are the initial and fluctuating components of temperature, and P is the kinematic pressure. We non-dimensionalize these equations such that length is in units of the layer height (L_z), temperature is in units of the initial temperature jump across the layer ($\Delta T_0 = L_z\partial_z T_0$), and velocity is in units of the freefall velocity ($v_{\text{ff}} = \sqrt{\alpha g L_z^2 \partial_z T_0}$). By these choices, one time unit is a freefall time ($t_{\text{ff}} = L_z/v_{\text{ff}}$). We introduce a reduced kinematic pressure, $\varpi \equiv (P/\rho_0 + \phi + |\boldsymbol{u}|^2/2)/v_{\text{ff}}^2$, where the gravitational potential, ϕ, is defined such that $\boldsymbol{g} = -\nabla\phi$. In non-dimensional form, and substituting $\boldsymbol{u}\cdot\nabla\boldsymbol{u} = \nabla(|\boldsymbol{u}|^2/2) - \boldsymbol{u}\times(\nabla\times\boldsymbol{u})$ and $\nabla^2\boldsymbol{u} = -\nabla\times(\nabla\times\boldsymbol{u})$, Eqns. 3 & 4 become

$$\frac{\partial \boldsymbol{u}}{\partial t} + \nabla\varpi - T_1\hat{z} + \mathcal{R}\nabla\times\boldsymbol{\omega} = \boldsymbol{u}\times\boldsymbol{\omega}, \tag{5}$$

$$\frac{\partial T_1}{\partial t} - \mathcal{P}\nabla^2 T_1 + w\frac{\partial T_0}{\partial z} = -\boldsymbol{u}\cdot\nabla T_1, \tag{6}$$

where $\boldsymbol{\omega} = \nabla\times\boldsymbol{u}$ is the vorticity. The dimensionless control parameters $\mathcal{R}$ and $\mathcal{P}$ are set by the Rayleigh (Ra) and Prandtl (Pr) numbers,

$$\mathcal{R} \equiv \sqrt{\frac{\text{Pr}}{\text{Ra}}}, \qquad \mathcal{P} \equiv \frac{1}{\sqrt{\text{Pr}\,\text{Ra}}}, \qquad \text{Ra} = \frac{g\alpha L_z^4 \partial_z T_0}{\nu\kappa} = \frac{(L_z\,v_{\text{ff}})^2}{\nu\kappa}, \qquad \text{Pr} = \frac{\nu}{\kappa}. \tag{7}$$

We hold Pr = 1 constant throughout this work, such that $\mathcal{P} = \mathcal{R}$. $\mathcal{P}$ and $\mathcal{R}$ are related to the inverse Reynolds and Peclet numbers of the evolved flows.

In Eqns. (2), (5), & (6), linear terms are grouped on the left-hand side of the equations, while nonlinear terms are found on the right-hand side. We timestep linear terms implicitly, and nonlinear terms explicitly. We utilize the Dedalus[1] pseudospectral framework [18] to evolve Eqns. (2), (5), & (6) forward in time using an implicit-explicit (IMEX), third-order, four-stage Runge-Kutta timestepping scheme RK443 [19].

Variables are time-evolved on a dealiased Chebyshev (vertical) and Fourier (horizontal, periodic) domain in which the physical grid dimensions are 3/2 the size of the coefficient grid. We study 2D and 3D convection in which the domain is a cartesian box, whose dimensionless vertical extent is $z \in [-1/2, 1/2]$, and which is horizontally periodic with an extent of $x, y \in [0, \Gamma]$, where $\Gamma = 2$ is the aspect ratio, as has been previously studied [10, 20]. In 2D simulations, we set $v = \partial_y = 0$. We specify no-slip, impenetrable boundary conditions at both the top and bottom boundary,

$$u = v = w = 0 \text{ at } z = \pm 1/2, \tag{8}$$

and we use mixed thermal boundary conditions, such that

$$T_1 = 0 \text{ at } z = +1/2, \qquad \frac{\partial T_1}{\partial z} = 0 \text{ at } z = -1/2. \tag{9}$$

For this choice of boundary conditions, the critical value of Ra at which the onset of convection occurs is $\mathrm{Ra_{crit}} = 1295.78$ [21], and the supercriticality of a run is defined as $S \equiv \mathrm{Ra}/\mathrm{Ra_{crit}}$. Studies of convection which aim to model astrophysical systems such as stars often employ mixed thermal boundary conditions, as we do here [12, 22, 23]. Our choice of the thermal boundary conditions in Eqn. (9) was motivated by the fact that accelerated evolution is simpler when both the thermal profile and the flux through the domain are fixed at a boundary.

The initial temperature profile is linearly unstable, $T_0(z) = -z$. On top of this profile, we fill T_1 with random white noise whose magnitude is $10^{-6}\mathcal{P}$, and which is vertically tapered so as to match the thermal boundary conditions. This ensures that the initial perturbations are much smaller than the evolved convective temperature perturbations, even at large Ra. We filter this noise spectrum in coefficient space, such that only the lower 25% of the coefficients have power; this low-pass filter is used to avoid populating the highest wavenumbers with noise in order to improve the stability of our spectral timestepping methods.

III. THE METHOD OF ACCELERATED EVOLUTION

Here we describe a method of Accelerated Evolution (AE), which we use to rapidly evolve the thermodynamic state of convective simulations. We compare this AE method to Standard Evolution (SE), in which we evolve the atmosphere from noise initial conditions for one thermal diffusion time, $t_\kappa = \mathcal{P}^{-1}$. Both AE and SE simulations begin with identical initial conditions, as described in section II. As Ra increases, and $\mathcal{P}$ decreases, SE solutions become intractable, while the timeframe of convergence for an AE solution remains nearly constant in simulation freefall time units (see table I in appendix A).

We study in depth a 2D simulation at $S = 10^5$ to demonstrate the power of AE. We compare kinetic energy (KE, black line) and mean temperature (blue line) traces from a SE run in Fig. 1a to an AE run in Fig. 1c. In Fig. 1a, the time evolution of the SE simulation is shown. The KE grows exponentially from white noise during the first ~ 25 t_{ff}. The solution then saturates and begins to slowly equilibrate towards the proper isothermal profile in the interior of the domain. This slow equilibration is evident in the behavior of the blue line, which measures $\langle T \rangle - T_{\mathrm{top}}$, where $\langle T \rangle$ is the volume-average of T, and $T_{\mathrm{top}} = -0.5$ is the temperature at the upper boundary. The mean atmospheric temperature and kinetic energies are fully converged when $t = 4000\ t_{\mathrm{ff}} = 0.35\ t_\kappa$. We show roughly the first thousand freefall time units of evolution, as well as the evolved thermodynamic state reached after a full thermal time of evolution. In Fig. 1c, similar traces are shown for the corresponding AE solution at the same parameters. The same linear growth phase occurs, but shortly after the peak of convective transient we accelerate the convergence of the atmosphere through the process which we describe below. We adjust the 1D vertical profile of the atmosphere three times, as denoted by the three labeled arrows in the graph numbered 1-3. After the third profile adjustment, we find that the atmosphere is nearly in its converged state and we begin to sample the evolved convective dynamics.

The horizontally averaged profiles of the vertical conductive flux, $\mathrm{F}_\kappa = \langle -\kappa \nabla (T_0 + T_1) \rangle_{x,y}$, and the vertical convective enthalpy flux, $\mathrm{F_E} = \langle w(T_0 + T_1) \rangle_{x,y}$, are the basis of the AE method. Here we use $\langle \rangle_{x,y}$ to represent a horizontal average. We measure both of these fluxes early in a simulation, retrieving profiles such as those shown in Fig. 1b.

---

[1] http://dedalus-project.org/

As the atmosphere evolves towards the isothermal profile specified by the upper (cold) boundary condition, excess temperature throughout the atmosphere must leave the domain. This excess thermal energy leaves through the upper boundary, as seen in Fig. 1b, where the amount of flux exiting at the top of the domain is nearly 20 times larger the flux entering the bottom of the domain. Once the atmospheric temperature profile reaches its evolved state, the flux entering the bottom boundary is equal to the flux exiting through the upper boundary. In general, this evolution is slow in SE (Fig. 1a), but AE (Fig. 1c) can rapidly advance a system whose fluxes are in a strongly disequilibrium state (Fig. 1b), into a near-equilibrium state, as shown in Fig. 1d. In this final state both boundaries conduct the same amount of flux. The converged state achieved through AE is at most 5% different from the SE solution, as shown in Fig. 1e. This is a very small difference considering the short timescales on which convergence is reached and the strongly disequilibrium state used to inform the AE process.

In order to adjust the temperature profle to achieve AE, we calculate the total flux, $F_{tot} = F_E + F_\kappa$, and then derive the profiles

$$f_E(z) = \frac{F_E}{F_{tot}}, \qquad f_\kappa(z) = \frac{F_\kappa}{F_{tot}}, \tag{10}$$

which have the systematic asymmetries (Fig. 1b) removed. These profiles describe which parts of the atmosphere depend on convection to carry flux (where $f_E(z) = 1$ and $f_\kappa(z) = 0$). We presume that the early convection occupies roughly the same volume as the evolved convection, and thus that the extent of the early thermal boundary layers (where $f_\kappa(z) = 1$ and $f_E(z) = 0$) will not change significantly over the course of the atmosphere's evolution. Under this assumption, in order to reach the converged state, the flux through the atmosphere must be decreased by some amount,

$$\xi(z) \equiv \frac{F_B}{F_{tot}}, \tag{11}$$

where $F_B = \mathcal{P}$ is the amount of flux that enters the bottom of the atmosphere.

In a time-stationary state, the horizontal- and time-average of Eqns. (5) and (6), neglecting terms which vanish due to symmetry, are

$$\frac{\partial}{\partial z} \langle \varpi \rangle_{x,y} - \langle T_1 \rangle_{x,y} \hat{z} = \langle \boldsymbol{u} \times \boldsymbol{\omega} \rangle_{x,y,\,ev}, \tag{12}$$

$$\frac{\partial}{\partial z} F_{E,\,ev} - \mathcal{P} \frac{\partial^2}{\partial z^2} \langle T_1 \rangle_{x,y} = 0. \tag{13}$$

Here, we construct $\langle \boldsymbol{u} \times \boldsymbol{\omega} \rangle_{x,y,\,ev} = \xi(z) \langle \boldsymbol{u} \times \boldsymbol{\omega} \rangle_{x,y}$ and $F_{E,\,ev} = \xi(z) F_E$ from our unevolved state, and solve for $\langle \varpi \rangle_{x,y}$ and $\langle T_1 \rangle_{x,y}$. Convective flows are perturbations around a thermal profile defined by these equations in the proper evolved, statistically stationary state. Furthermore, under the proper specification of $F_{conv,\,ev}$ and $\langle \boldsymbol{u} \times \boldsymbol{\omega} \rangle_{x,y,\,ev}$, *the mean thermodynamic structure of the system is fully specified.*

Thus, the AE method occurs in the following steps. First, we pause a convective simulation and construct $\xi(z)$ from measured flux profiles in the convective domain. We solve a 1D boundary value problem consisting of Eqns. (12) & (13) to obtain the proper evolved thermodynamic profile, and proper conductive flux. To obtain the proper convective enthalpy flux, we multiply both the velocity field, $\boldsymbol{u}$, and the temperature perturbations around the mean profile, $T - \langle T \rangle_{x,y}$, by $\sqrt{\xi}$; this diminishes the magnitude of these perturbations, and the flux they carry, appropriately. After adjusing the fields of a simulation in this manner, we continue timestepping forward. For specifics on the precise implementation of the AE method, we refer the reader to appendix B.

IV. RESULTS

We study evolved standard evolution (SE) solutions whose supercriticalities (S) are $S \in (1, 10^5]$ in 2D and $S \in (1, 10^4]$ in 3D. We compare their properties to accelerated evolution (AE) runs at $S \in (1, 10^7]$ in 2D and $S \in (1, 10^4]$ in 3D. We refer the reader to appendix A for a full list of simulations.

The Nusselt number (Nu) quantifies the efficiency of convective heat transport and is defined as

$$Nu = \frac{\langle F_{conv} + F_{cond} \rangle}{\langle F_{cond,\,ref} \rangle} = \frac{\langle wT - \mathcal{P}\partial_z T \rangle}{\langle -\mathcal{P}\partial_z T \rangle}, \tag{14}$$

where the volume average of a quantity, η, is shown as $\langle \eta \rangle$. When $S < 10^{3+2/3}$ in 2D and for all runs in 3D, the evolved system is characterized by a time-stationary value of Nu, and is thus in a state of constant convective heat transport.
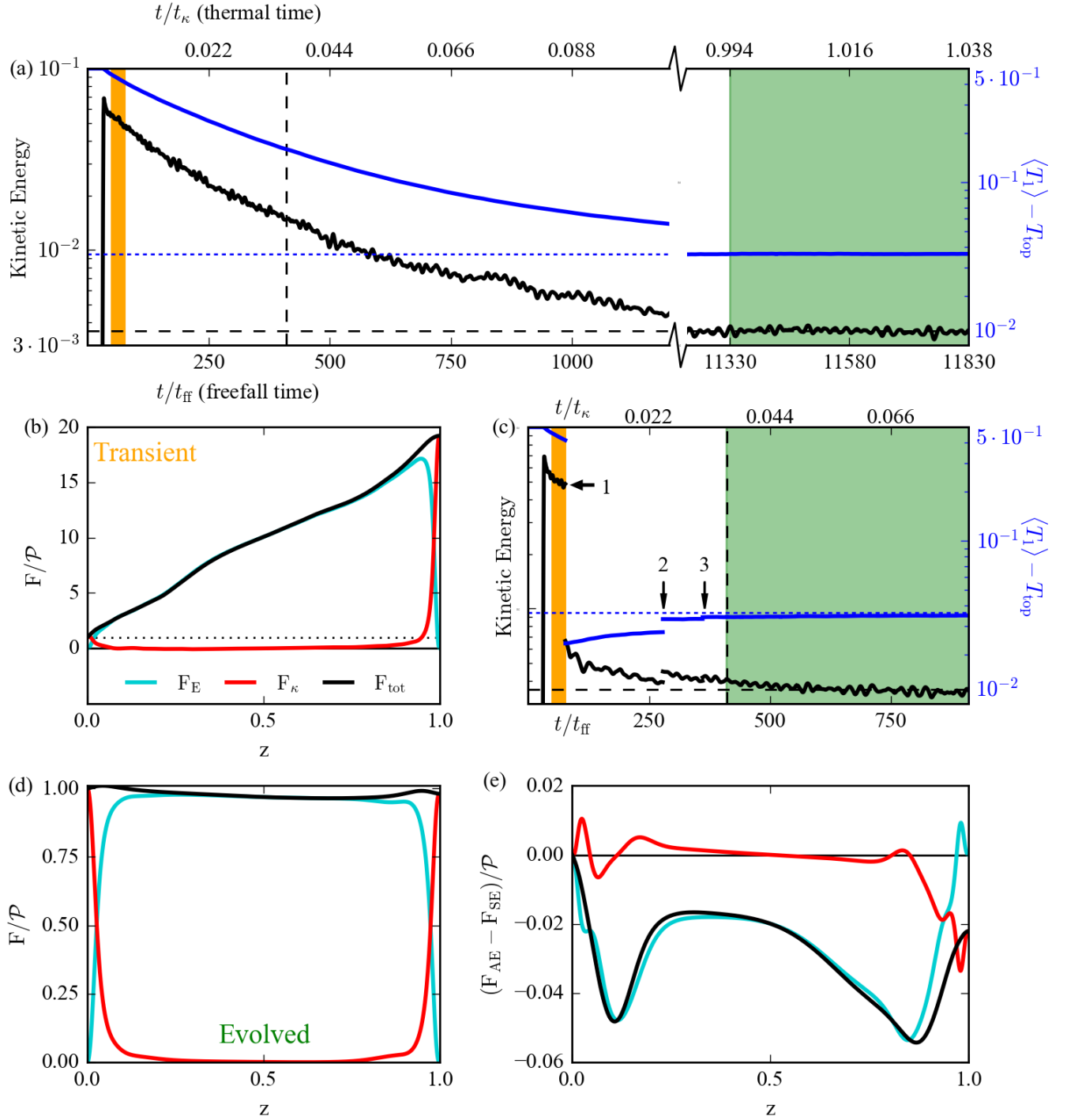
FIG. 1. (a) Kinetic energy (black) and $\langle T \rangle - T_{\text{top}}$ (blue) vs. time are shown for a SE run at $S = 10^5$. The mean evolved values of kinetic energy and mean temperature, averaged over the time shaded in green, are denoted by the horizontal dashed lines. (b) The time- and horizontally-averaged flux profiles are shown for the times highlighted in orange in (a). (c) The same quantities as in (a) are shown, but for AE at the same parameters. The axes are scaled identically in (a) and (c), and the AE method is used three times, marked by the numbered arrows. The fluxes averaged over the green shaded region of (c) are shown in (d). The difference between the fluxes in the AE and SE solutions is shown in (e).
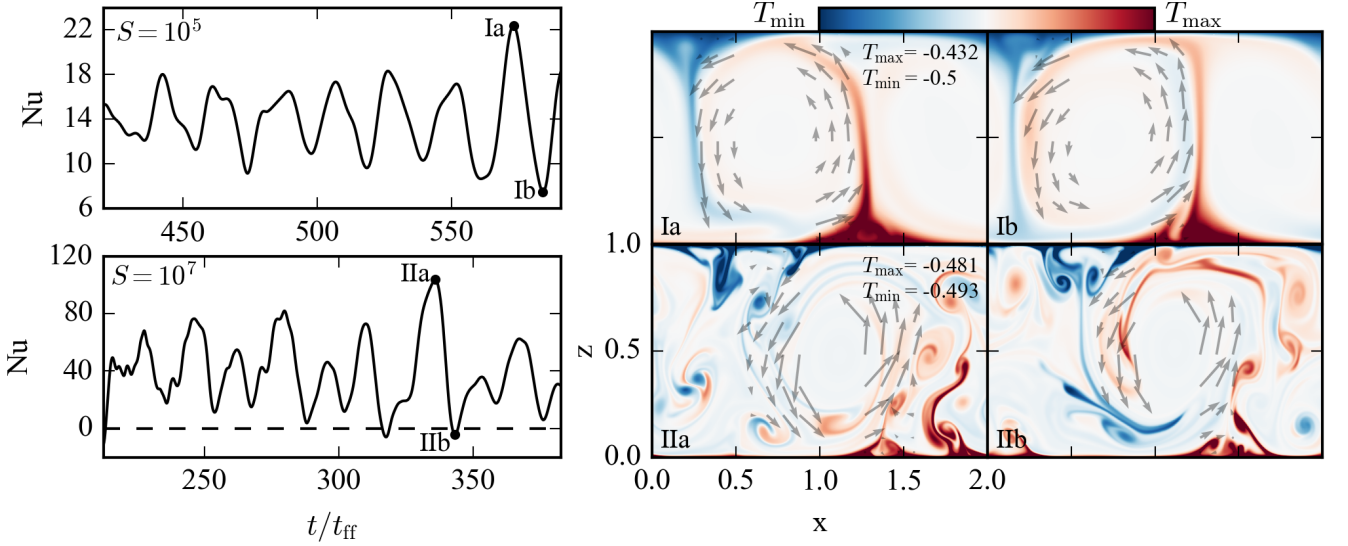
FIG. 2. The time variation of the Nusselt number is shown for two AE cases at $S = 10^5$ (top) and $S = 10^7$ (bottom). On the left, the instantaneous value of Nu is shown as a function of time. On the right, temperature snapshots are shown for Nu maxima (Ia & IIa) and minima (Ib & IIb). The suppressed value of Nu at the minma arises from entrainment of fluid elements whose temperature perturbations are wrongly signed (e.g., hot material going downwards and cold material going upwards in Ib & IIb). The colorbar scaling of panels Ia&b are the same, as are the scalings of panels IIa&b. The minimum temperature is chosen by the fixed-temperature boundary condition at the top, $T_{top} = -0.5$. The decreased range of the colorbar scaling for for IIa&b was chosen to better display the convective dynamics.

At larger S in 2D, the value of Nu varies significantly over time, as shown by the time traces for $S = 10^5$ (top, left) and $S = 10^7$ (bottom, left) for two AE runs in Fig. 2. We find that these systems exhibit large Nu during states in which temperature fluctuations travel in their natural buoyant direction (Fig. 2, Ia & IIa, where cold elements fall and hot elements rise). However, when wrongly-signed temperature perturbations are entrained in an upflow or downflow with oppositely signed fluid, Nu is suppressed (Fig. 2, Ib and IIb, where warm fluid is pulled down by the downflow lane, and cool fluid is drawn up by the upflow lane). The plumes in these systems naturally oscillate horizontally over time, switching between transport being dominated by a counterclockwise cell, as pictured in Fig. 2, and a clockwise cell. Our choice of no-slip boundary conditions prevents the fluid from entering a full domain shearing state [20], and the oscillatory nature of the plumes is stable. However, thanks to our choice of periodic boundary conditions and despite the no-slip conditions, the full system of the upflow and downflow plumes is free to slowly migrate to the left or right over time, and we observe this phenomenon in our solutions. The 2D SE simulations exhibit the same horizontally oscillatory behavior as the AE solutions for the same initial conditions. This time-dependent behavior of Nu is not seen strongly in our 3D solutions, however most 3D simulations we conducted were at low S compared to the runs in which this behavior was observed in 2D.

The time- and volume-averaged values of Nu, the RMS Reynolds number (Re), and the mean temperature are shown for AE solutions in Fig. 3a-c. Mean values are shown by the symbols (purple circles and red stars), and the vertical lines represent the standard deviation of the measurement over time. Nu is shown as a function of Ra and S in Fig. 3a. The dynamic nature of the plume structures (e.g., Fig. 2) diminishes the mean scaling of the heat transport to Nu $\propto$ Ra$^{1/5}$, which is weaker than classic scaling laws [10, 24]. Previous studies in 2D convection may have avoided these time-varying Nu states by using bootstrapping techniques as initial conditions for high S runs. In Fig. 3b, we report Re $= \langle |\boldsymbol{u}| \rangle / \mathcal{R}$ as a function of Ra and S. Re measures the degree of turbulence in the solution, and scales roughly as Re $\propto$ Ra$^{0.45}$. Each simulation shows little variance in the value of Re over time. Fig. 3c shows the scaling of $\langle T \rangle - T_{top}$, the mean value of the temperature minus its value at the upper (fixed temperature) boundary. The average temperature, $\langle T \rangle$, is dominated by its value in the isothermal interior, so this measurements serves as a probe of the temperature jump across the boundary layers. As a result, we expect this measure to scale inversely with Nu in converged solutions where fixed-flux boundary conditions are used [25]. We find here that $(\langle T \rangle - T_{top}) \propto$ Ra$^{-1/5}$, precisely the inverse scaling of Nu.

In Fig. 3d-f, we report the fractional difference between measurements in the AE and SE solutions. The mean values of Nu and $\langle T \rangle - T_{top}$ measured in AE are accurate to SE values to within $\sim 1\%$. Re measurements show marginally greater error, with AE measurements being $\leq 2\%$ different from SE measurements.

For the select 3D runs conducted in this study, the scaling of Nu, Re, and $\langle T \rangle - T_{\text{top}}$ reported in Fig. 3a-c is nearly identical to the 2D simulations. Errors between AE and SE solutions in 3D fall within the same range as errors in 2D in Fig. 3d-f. AE is therefore equally effective in both 2D and 3D, and we restrict much of our study to 2D here in order to more thoroughly sample paramtere space.

The measurements presented in Fig. 3 demonstrate that AE can be powerfully employed in parameter space studies in which large numbers of simulations are compared in a volume-averaged sense. We now turn our examination to a more direct comparison of AE and SE for 2D convection at $S = 10^5$, the time and flux evolution of which was shown in Fig. 1. All comparisons that follow for these two runs occur over the times shaded in green in Fig. 1a&c. Measurements are sampled every 0.1 freefall time units for 500 total freefall time units.

As AE is fundamentally a 1D adjustment to the thermodynamic structure of the solution, we compare the horizontally- and time-averaged temperature profiles attained by AE and SE in Fig. 4a. The boundary layer width and structure are nearly identical between the two solutions, but the the mean temperature in the isothermal interior differs by roughly 0.5% (Fig. 4c).

The probability distribution functions (PDFs) of point-by-point temperature measurements are compared for the two runs in Fig. 4b. To construct these PDFs, we interpolate the full temperature field at each measurement time onto an evenly spaced grid, determine the frequency distribution of all T values over the duration of the 500 t_{ff} measurement window, and then normalize the distribution such that its integral is unity. The two PDFs have noticeably different modes, as is expected from Fig. 4a. Over long timescales, the 0.5% difference between the two profiles would disappear, as the AE solution evolves to be exactly the SE solution; this is evident in the asymmetry of the AE PDF near the mode in Fig. 4b and also the trend of the mean temperature over time in Fig. 1c.

One means of comparing two PDFs to determine if they are drawn from the same underlying sample distribution is through the use of a Kolmogorov-Smirnov (KS) test [26]. We calculate the KS statistic for a PDF of some value, q, as

$$\text{KS}(q) = \text{CDF}_{\text{AE}}(q) - \text{CDF}_{\text{SE}}(q), \tag{15}$$
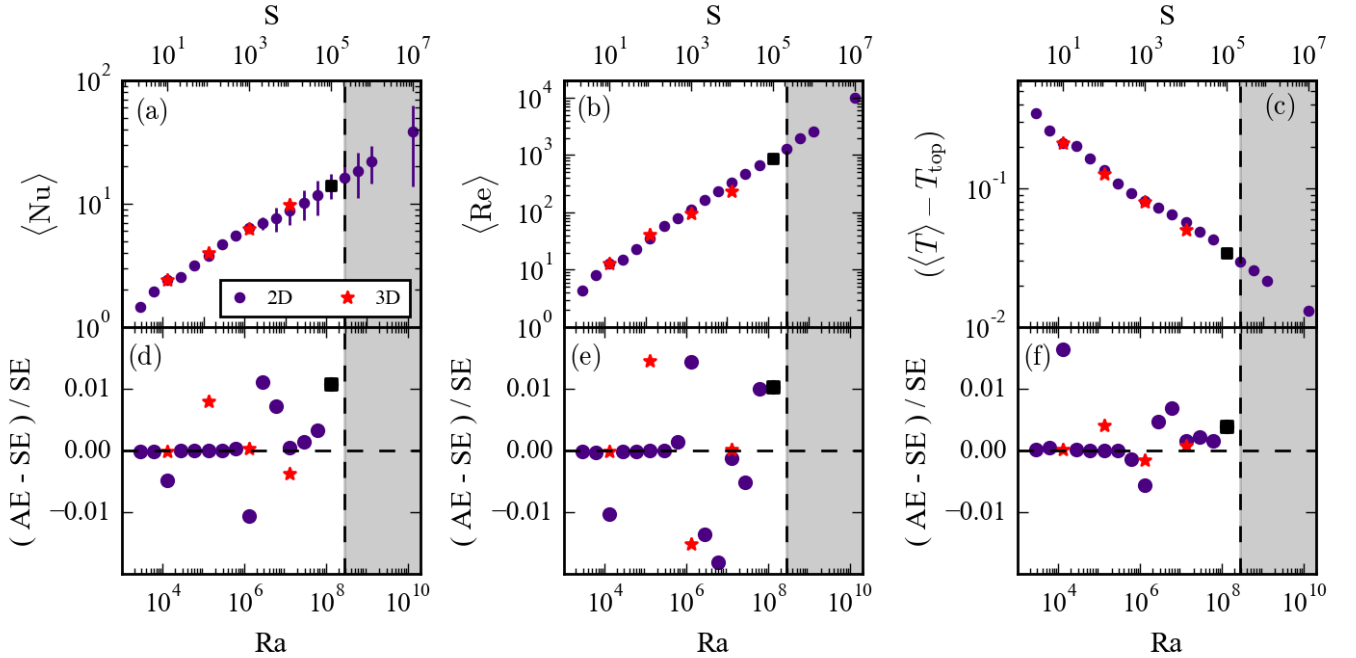

FIG. 3. Volume- and time-averaged measurements of the Nusselt number (Nu), the RMS Reynolds number (Re), and the mean temperature ($\langle T \rangle$) for AE runs are shown in (a)-(c). Symbols are located at the mean value of each measurement and denote 2D (purple circles) and 3D (red stars). The run at $S = 10^5$ marked as a black square is examined in more detail in Figs. 1, 2, 4, & 5. Vertical lines represent the standard deviation of the measurement, and quantify natural variation over the averaging window. (a) Nu scales as $\text{Ra}^{1/5}$; at high S in 2D the value of Nu fluctuates over time (see Fig. 2). (b) Re, which measures turbulence in the solution, scales as $\text{Ra}^{0.45}$. (c) The difference between $\langle T \rangle$ and the value of T at the fixed-temperature top boundary is shown; this quantity scales as $\text{Ra}^{-1/5}$, the inverse of Nu. Relative error for measurements of (d) Nu, (e) Re, and (f) $\langle T \rangle - T_{\text{top}}$ between AE solutions and SE solutions are shown. The greyed area of the plots indicates the region in which only AE runs were carried out due to computational expense.
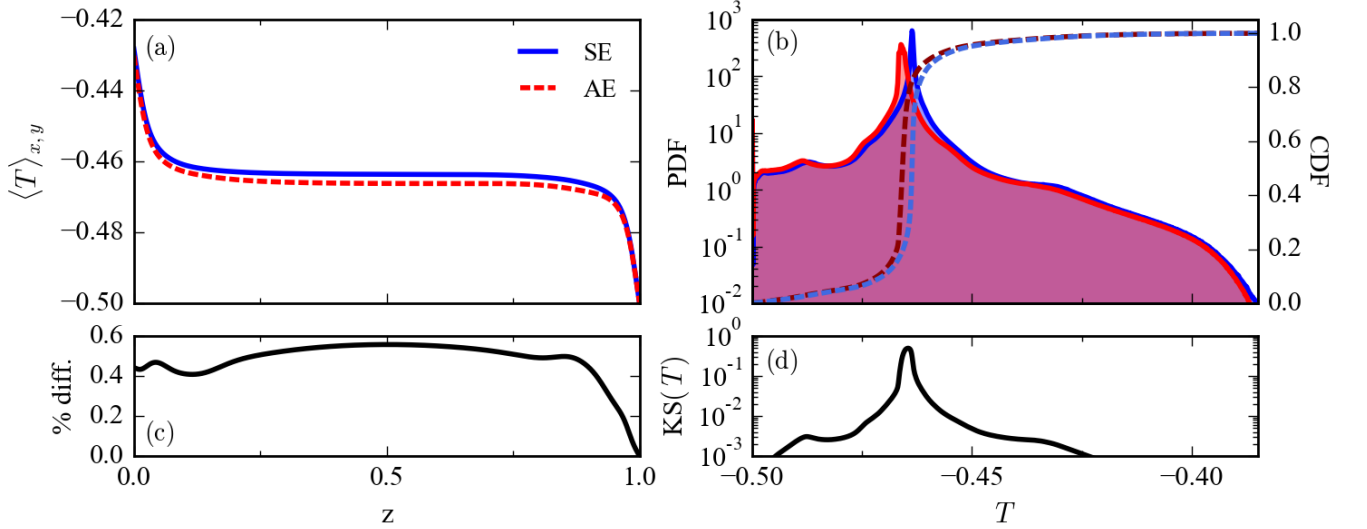
FIG. 4. Comparisons of the evolved thermodynamic states of an AE and SE run at $S = 10^5$ are shown. (a) Evolved horizontally- and time-averaged temperature profiles, as a function of height. (b) Probability Distribution Functions (PDFs) and their integrated Cumulative Distribution Functions (CDFs) of point-by-point measurements of the temperature field. (c) The percentage difference between the mean temperature profiles as a function of height. The difference between the mean profiles is very small, O(0.5%). (d) KS(T), as defined in Eqn. **??**, is shown. The small difference in the mean interior temperature between AE and SE results in a large difference between the two temperature distributions near the values of the temperature modes. The spread of temperature around the modes, which includes the fluctuations that drive convection, are nearly identical between the two runs.

where CDF stands for cumulative distribution function, the integral of the PDF. A traditional Kolmogorov-Smirnov statistic is just a single value, $\overline{KS(q)} = |KS(q)|_\infty = \max|KS(q)|$, and we use both the profile KS(q) and $\overline{KS(q)}$ to gain insight into the likeness of two PDFs. We show KS(T) in Fig. 4d, and the CDFs used to construct it overlay the PDFs in Fig. 4b. Near the modes of the temperature PDFs, $\overline{KS(T)} = 0.495$, which is very large and implies that roughly half of all measurements in the AE case are at a lower T than those in the SE case. While this difference is significant, it is also expected from Fig. 4a. Fortunately, KS(T) is very small away from the modes, indicating that the temperature fluctuations off of the modes, which are the primary drivers of convective transport, are nearly identical.

In addition to comparing the thermodynamic state achieved by the SE and AE methods, we examine the velocities and heat transport found in the evolved states. Shown are the PDFs of vertical velocity (w, Fig. 5a), horizontal velocity (u, Fig. 5b), and the nonlinear vertical convective flux ($w(T - \langle T \rangle_{x,y})$, Fig. 5c). Each PDF here shows a strong peak near zero due to the no-slip, impenetrable velocity boundary conditions (Eqn. (8)). The CDFs of each profile are overplotted, and corresponding KS profiles are shown in Fig. 5d-f. We report $\overline{KS(w)} = 0.00615$, $\overline{KS(u)} = 0.0349$, and $\overline{KS(w(T - \langle T \rangle_{x,y}))} = 0.0263$. The difference in vertical velocity and heat transport between AE and SE is negligible, which is unsurprising in light of the Nu measurements of Fig. 3a&d. this also confirms that the large $\overline{KS(T)}$ in Fig. 4d is not of concern, and that the AE run achieves the proper convective solution. The horizontal velocity shows some small deviation between the two simulations, and this likely relates to the precise configuration of the convective plumes (e.g., Fig. 2). We find that the difference in KS(u), which consistently has more probability of flows moving left (in the -x direction), appears to be caused by a more prominent migration of the full roll system in the -x direction in the AE run than in the SE run. This migration does not appear to affect the vertical transport appreciably.

The small differences between the SE and AE solutions for the case studied in Figs. 1, 4, & 5, show the extreme power of AE. In addition to the fact that AE runs require much less total simulation time (see e.g., Fig. 1a&c and the time values in the green highlighted regions), the first application of AE in a given simulation (Fig. 1c, at the arrow labeled "1") drastically increases the average timestep by immediately progressing the simulation into a more converged state. For the $S = 10^5$ case we examined in detail, the average time step grew by a factor of 2-3 due to the decreased convective velocities from the transient state to the evolved state. At $S = 10^7$, the AE solve immediately improved the timestep size by nearly a factor of 4. Thus, AE achieves converged solutions in few simulation time units, while also taking less real world time per simulation time unit, when compared to the slowly converging SE
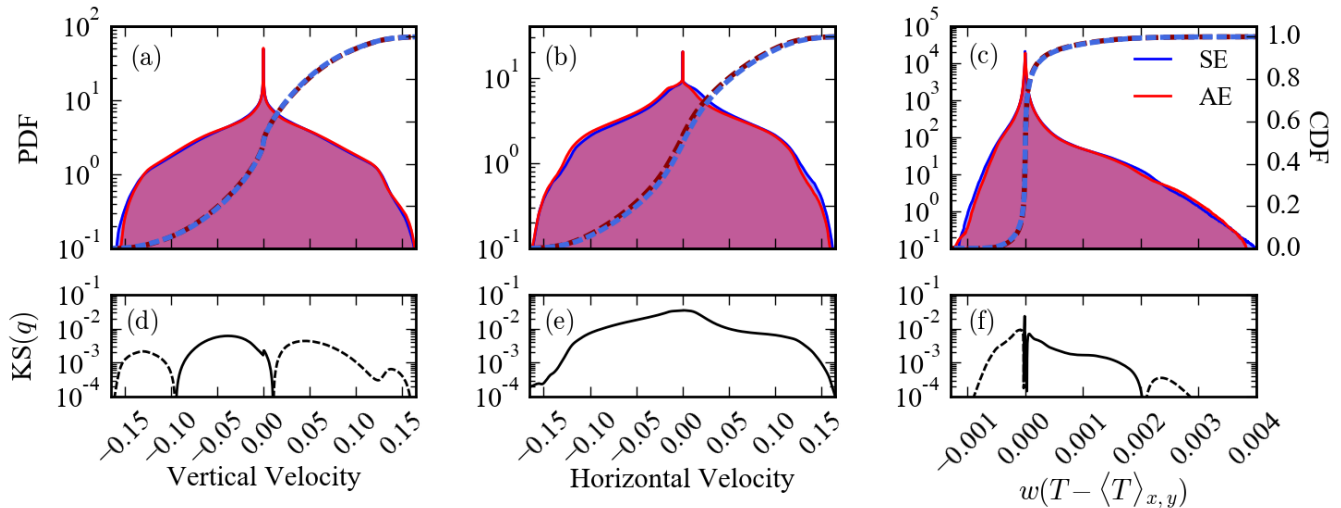
FIG. 5. Probability distribution functions (PDFs) of (a) the vertical velocity, (b) the horizontal velocity, and (c) nonlinear convective transport are shown for 2D runs achieved through SE (blue) and AE (red) at $S = 10^5$. The cumulative distribution function (CDF) is overplotted for each PDF. (d-f) The KS profiles, as defined in Eqn. (15), are shown for the related distributions; solid lines indicate positive values while dashed lines are negative values. Unlike the temperature distributions in Fig. 4, these distributions show very good agreement and small values of the KS statistic.

state at the same simulation time.

V. EXTENSIONS & CONCLUSIONS

In this work we have studied a method of Accelerated Evolution (AE) which can be employed to achieve rapid thermal convergence of convective simulations. We compared this technique to the Standard Evolution (SE) of convection through a full thermal diffusion timescale, and we showed that AE rapidly obtains solutions whose dynamics are statistically similar to SE solutions. The AE method is valid at low values of S, where SE solutions converge quickly due to the short thermal timescale, and AE remains applicable at high values of S, where SE solutions are intractable. As discussed, AE is equally applicable in 2D and 3D; here we have restricted most of our study to 2D to extend our parameter space coverage. At the largest values of S in which AE and SE are compared in this work, we find time savings of nearly an order of magnitude. For example, in 2D and at $S = 10^5$, the AE run took 10.78 wall hours on 256 cores ($2.8 \cdot 10^3$ cpu-hours) while the SE run took 94 wall hours ($2.4 \cdot 10^4$ cpu-hours). In 3D and at $S = 10^4$, the AE run took 2.81 wall hours on 8192 cores ($2.3 \cdot 10^4$ cpu-hours), while the SE run took 37.9 wall hours, or ($3.1 \cdot 10^5$ cpu-hours). As S increases, and the thermal time, t_κ, simultaneously increases, we anticipate the computational and wall hour time savings to further increase. The additional computational expense of 3D runs compared to 2D runs implies that 3D studies can greatly benefit from the proper implementation of AE.

Here we studied Rayleigh-Bénard convection as a test case for the AE method, but we argue that the true power of this technique is in its extensions to more complicated studies. To achieve AE in more complicated systems, one need only derive the steady-state, horizontally-averaged equations governing the convective dynamics (e.g., the analogs to Eqns. (12) & (13)) and couple those equations with knowledge of the boundary conditions and current dynamics as described in section III and appendix B. While in-depth studies of AE extensions are beyond the scope of this paper, we will briefly discuss avenues in which AE should be explored and tested in order to push interesting studies of various convective phenomena into the astrophysically-interesting, high-Ra regime.

Convection in natural systems is often driven by internal heating processes rather than imposed, fixed boundary conditions. The AE procedure can be straightforwardly applied to Boussinesq studies of internally heated convection [21], where a constant source term in the energy equation causes the vertical flux through the system to increase with height. In these systems, the thermal evolution is very slow compared to convective dynamical timescales, just as it is in classic Rayleigh-Bénard convection. These systems can be studied using exactly the methods that we examined here, but multiplying the flux profiles derived in Eqn. (10) by the proper, height-dependent flux. Studies of convection in natural systems often employ height-dependent conductivities [27, 28], leading to natural flux divergences that act as internal heating terms. The study of AE in the context of simple internal heating simulations will be an important

step towards achieving AE in simulations with astrophysically realistic conductivities. As such studies (e.g., [28]) are currently very limited in the span of Ra that can be examined, AE could be key in studying the scaling of convective properties in such systems, and gaining knowledge about the eventual, very-high-Ra, ultimate regime of such systems.

A further area which could benefit from AE is overshooting convection, in which studies examine adjacent stable and convecting regions [13, 14, 16]. When the interface between the stable region and the convecting region is stiff, convective motions cannot accelerate the restratification of the stable region. In fully-convective domains, such as those studied in this work, the thermodynamics evolve at a more rapid rate than the thermal diffusion time across the domain due to convective mixing. For example, in Fig. 1a, the SE solution is fully converged after $4 \cdot 10^3$ frefall time units, which is roughly 35% of a thermal timescale. However, in studies where there is a stable region which is not mixed by convection, the experimentalist must either wait through a thermal diffusion time or otherwise manually adjust the initial profile to study converged dynamics [13]. In these systems, AE can instantaneously adjust the thermal profile in the stable region from a far-disequilibrium state to the properly converged solution, skipping the slow thermal evolution.

Studies of stratified, compressible convection have much to gain through developing and employing AE. In many studies of stratified convection, the thermal diffusivity is a non-constant coefficient and varies inversely with density [7]. Thus, the thermal timescale increases with depth in the atmosphere, and the difficulty of achieving thermal convergence grows as simulators study more highly stratified domains. For example, in a modestly stratified atmosphere which spans three density scale heights, the density at the bottom, and thus the thermal timescale, is a factor of 20 greater than at the top of the domain. In order to extend AE into this regime, two additional pieces of information must be considered. First, rather than constructing the profiles in Eqn. (10) with the total flux through the domain, only the superadiabatic portion of the flux should be considered [7]. Second, in addition to solving for hydrostatic balance and thermal equilibrium, as in Eqns. (12) & (13), it is essential to simultaneously evolve the density profile in a manner which conserves mass. In a 1D boundary value problem, such as is solved to achieve AE here, this implies the inclusion of an equation which tracks the vertically integrated mass, and sets boundary conditions on that mass to ensure that no mass enters or leaves the domain.

AE techniques can contribute to improving the description of convection in stellar evolution codes. Current state of the art stellar structure models are solutions of 1D simulations which parameterize convection using Mixing Length Theory and its variants [29–32]. Recent studies [3–5, 33, 34] have tried to understand how to simultaneously resolve convective motions and evolve systems through many thermal timescales, as is required when determining the interior structure of stars over their evolving lifetimes. We now know that implicit timestepping methods must resolve convective motions in order to timestep with stability [3–5], and thus cannot achieve fast, meaningful system evolution. Other efforts have begun to project the results of 3D simulations into 1D models to more properly parameterize convection for stellar evolution [33, 34], but the validity of these 321D techniques has not been hitherto thoroughly tested. This is precisely the technology employed in the tested AE method we present here. Through the careful expansion of AE from Rayleigh-Bénard convection to fully stratified, compressible convection with realistic opacities, it is possible that carefully evolved stellar structure models which use statistics from resolved convective motions are well within reach of modern computing resources.

Appendix A: Table of Runs

In Table I we list key properties of all simulations conducted in this work.

TABLE I. Simulation parameters. We report the supercriticality (S), Rayleigh number (Ra), and coefficient resolution (nz, nx, and ny are the number of coefficients in the z, x, and y directions respectively). Simulation run times required to reach convergence are reported for the SE solutions (t_{therm}) and the AE solutions (t_{AE}). The amount of time over which simulations measurements were taken in the evolved state is listed (t_{avg}). All times are in freefall time units. The volume-averaged Nusselt number (Nu) of the AE and SE solutions are shown. In the upper part of the table, information pertaining to 2D runs is reported, while information pertaining to 3D runs is in the lower part of the table.

S	Ra	nz	nx, ny	t_{therm}	t_{AE}	t_{avg}	$\mathrm{Nu_{SE}}$	$\mathrm{Nu_{AE}}$
				2D Runs				
$10^{1/3}$	$2.79 \cdot 10^3$	32	64	52.8	340	100	1.46	1.46
$10^{2/3}$	$6.01 \cdot 10^3$	32	64	77.6	282	100	1.95	1.95
10^1	$1.30 \cdot 10^4$	32	64	114	265	100	2.43	2.42
$10^{1+1/3}$	$2.79 \cdot 10^4$	32	64	167	251	100	2.54	2.54
$10^{1+2/3}$	$6.01 \cdot 10^4$	32	64	245	245	100	3.14	3.14
10^2	$1.30 \cdot 10^5$	64	128	360	326	100	3.8	3.8
$10^{2+1/3}$	$2.79 \cdot 10^5$	64	128	528	248	100	4.71	4.71
$10^{2+2/3}$	$6.01 \cdot 10^5$	64	128	776	251	100	5.5	5.5
10^3	$1.30 \cdot 10^6$	128	256	$1.14 \cdot 10^3$	268	200	6.4	6.33
$10^{3+1/3}$	$2.79 \cdot 10^6$	128	256	$1.67 \cdot 10^3$	247	500	6.87	6.95
$10^{3+2/3}$	$6.01 \cdot 10^6$	256	512	$2.45 \cdot 10^3$	275	500	7.54	7.59
10^4	$1.30 \cdot 10^7$	256	512	$3.60 \cdot 10^3$	301	500	8.83	8.83
$10^{4+1/3}$	$2.79 \cdot 10^7$	256	512	$5.28 \cdot 10^3$	317	500	10.13	10.14
$10^{4+2/3}$	$6.01 \cdot 10^7$	256	512	$7.76 \cdot 10^3$	326	500	11.65	11.69
10^5	$1.30 \cdot 10^8$	512	1024	$1.14 \cdot 10^4$	411	500	14.02	14.18
$10^{5+1/3}$	$2.79 \cdot 10^8$	512	1024	$1.67 \cdot 10^4$	391	500	—	16.21
$10^{5+2/3}$	$6.01 \cdot 10^8$	512	1024	$2.45 \cdot 10^4$	453	500	—	18.58
10^6	$1.30 \cdot 10^9$	1024	2048	$3.60 \cdot 10^4$	436	500	—	22.13
10^7	$1.30 \cdot 10^{10}$	2048	4096	$1.14 \cdot 10^5$	183	170	—	38.29
				3D Runs				
10^1	$1.30 \cdot 10^4$	32	64×64	114	261	100	2.42	2.42
10^2	$1.30 \cdot 10^5$	64	128×128	360	249	100	3.97	4
10^3	$1.30 \cdot 10^6$	128	256×256	$1.14 \cdot 10^3$	243	500	6.27	6.27
10^4	$1.30 \cdot 10^7$	256	512×512	$3.60 \cdot 10^3$	244	500	9.92	9.88

Appendix B: Accelerated Evolution Recipe

In order to achieve Accelerated Evolution (AE), we pause the Direct Numerical Simulation (DNS) which is evolving the dynamics of convection and solve a 1D Boundary Value Problem (BVP) consisting of Eqns. (12) & (13). After solving this BVP, we appropriately adjust the fields being evolved in the DNS towards their evolved state, and then we continue running the now-evolved DNS. The specific steps taken in completing the AE method are as follows:

1. Wait some time, $t_{\mathrm{transient}}$, before beginning the AE process.

2. During the DNS, calculate time averages of the 1D vertical profiles of F_E, F_{tot}, and $\langle \boldsymbol{u} \times \boldsymbol{\omega} \rangle_{x,y}$, updating them every timestep. To calculate these averages, we use a trapezoidal-rule integration in time, and then divide by the total time elapsed over which the average is taken.

3. Pause the DNS once the averages are sufficiently converged. To ensure that an average is converged, at least some time t_{min} must have passed since the average was started to ensure that the full range of convective dynamics are probed, and the profiles must change by no more than $P\%$ on a given timestep.

4. Construct ξ, $F_{E,\,\mathrm{ev}}$, and $\langle \boldsymbol{u} \times \boldsymbol{\omega} \rangle_{x,y,\,\mathrm{ev}}$, as specified in section III from the averaged profiles.

5. Solve the BVP for $\langle T_1 \rangle_{x,y}$ and $\langle \varpi \rangle_{x,y}$ of the evolved state. Set the horizontal average of the current DNS thermodynamic fields equal to the results of the BVP.

6. Multiply the velocity field, $\boldsymbol{u} = u\hat{x} + v\hat{y} + w\hat{z}$, and the temperature fluctuations, $T - \langle T \rangle_{x,y}$, by $\sqrt{\xi}$ in the DNS to properly reduce the convective flux.

7. Continue running the DNS.

We refer to this process as an "AE BVP solve."

While the use of a single AE BVP solve rapidly advances the convecting state to one that is closer to the evolved state, we find that repeating this method multiple times is the best way to ensure that the AE solution is truly converged. For all runs in 2D at $S < 10^5$, we set $t_{\text{transient}} = 50$, completed an AE BVP solve with $t_{\min} = 30$ and $P = 0.1$, and then repeated the procedure. For all 3D runs and 2D runs with $S \in [10^5, 10^6]$, we did a first AE BVP solve with $t_{\text{transient}} = 20$, $t_{\min} = 20$, and $P = 1$ in order to quickly reach a near- converged state and vastly increase our timestep size. After this first solve, we completed two AE BVP solves, with $t_{\text{transient}} = 30$, $t_{\min} = 30$, and $P = 0.1$ to get very close to the solution (as in Fig. 1c). At very high $S = 10^7$, we ran two AE BVP solves with $t_{\min} = 20$ and $P = 1$. For the first solve, we set $t_{\text{transient}} = 20$, and for the second we set $t_{\text{transient}} = 30$. We used fewer solves at this high value of S in part to reduce the computational expense of the run, and in part because a third BVP generally did not greatly alter the solution (as in Fig. 1c, arrow 3). We wait 50 freefall times after the final AE BVP solve of each run before beginning to take measurements.

[1] B. P. Brown, M. K. Browning, A. S. Brun, M. S. Miesch, and J. Toomre, "Persistent Magnetic Wreaths in a Rapidly Rotating Sun," Astrophys. J. **711**, 424–438 (2010), arXiv:1011.2831 [astro-ph.SR].
[2] N. A. Featherstone and B. W. Hindman, "The Spectral Amplitude of Stellar Convection and Its Scaling in the High-Rayleigh-number Regime," Astrophys. J. **818**, 32 (2016), arXiv:1511.02396 [astro-ph.SR].
[3] M. Viallet, I. Baraffe, and R. Walder, "Towards a new generation of multi-dimensional stellar evolution models: development of an implicit hydrodynamic code," Astronomy & Astrophysics **531**, A86 (2011), arXiv:1103.1524 [astro-ph.IM].
[4] M. Viallet, I. Baraffe, and R. Walder, "Comparison of different nonlinear solvers for 2D time-implicit stellar hydrodynamics," Astronomy & Astrophysics **555**, A81 (2013), arXiv:1305.6581 [astro-ph.SR].
[5] M. Viallet, T. Goffrey, I. Baraffe, D. Folini, C. Geroux, M. V. Popov, J. Pratt, and R. Walder, "A Jacobian-free Newton-Krylov method for time-implicit multidimensional hydrodynamics. Physics-based preconditioning for sound waves and thermal diffusion," Astronomy & Astrophysics **586**, A153 (2016), arXiv:1512.03662 [astro-ph.IM].
[6] D. Lecoanet, B. P. Brown, E. G. Zweibel, K. J. Burns, J. S. Oishi, and G. M. Vasil, "Conduction in Low Mach Number Flows. I. Linear and Weakly Nonlinear Regimes," Astrophys. J. **797**, 94 (2014), arXiv:1410.5424 [astro-ph.SR].
[7] E. H. Anders and B. P. Brown, "Convective heat transport in stratified atmospheres at low and high Mach number," Physical Review Fluids **2**, 083501 (2017), arXiv:1611.06580 [physics.flu-dyn].
[8] B. Bordwell, B. P. Brown, and J. S. Oishi, "Convective Dynamics and Disequilibrium Chemistry in the Atmospheres of Giant Planets and Brown Dwarfs," Astrophys. J. **854**, 8 (2018), arXiv:1802.03026 [astro-ph.EP].
[9] M. Stix, "On the time scale of energy transport in the sun," Solar Physics **212**, 3–6 (2003).
[10] H. Johnston and C. R. Doering, "Comparison of Turbulent Thermal Convection between Conditions of Constant Temperature and Constant Flux," Phys. Rev. Lett. **102**, 064501 (2009), arXiv:0811.0401 [physics.flu-dyn].
[11] R. Verzicco and R. Camussi, "Transitional regimes of low-Prandtl thermal convection in a cylindrical cell," Physics of Fluids **9**, 1287–1295 (1997).
[12] N. E. Hurlburt, J. Toomre, and J. M. Massaguer, "Two-dimensional compressible convection extending over multiple scale heights," Astrophys. J. **282**, 557–573 (1984).
[13] L.-A. Couston, D. Lecoanet, B. Favier, and M. Le Bars, "Dynamics of mixed convective-stably-stratified fluids," Physical Review Fluids **2**, 094804 (2017), arXiv:1709.06454 [physics.flu-dyn].
[14] A. Brandenburg, K. L. Chan, Å. Nordlund, and R. F. Stein, "Effect of the radiative background flux in convection," Astronomische Nachrichten **326**, 681–692 (2005), astro-ph/0508404.
[15] R. J. A. M. Stevens, D. Lohse, and R. Verzicco, "Prandtl and Rayleigh number dependence of heat transport in high Rayleigh number thermal convection," Journal of Fluid Mechanics **688**, 31–43 (2011), arXiv:1102.2307 [physics.flu-dyn].
[16] N. E. Hurlburt, J. Toomre, and J. M. Massaguer, "Nonlinear compressible convection penetrating into stable layers and producing internal gravity waves," Astrophys. J. **311**, 563–577 (1986).
[17] E. A. Spiegel and G. Veronis, "On the Boussinesq Approximation for a Compressible Fluid." Astrophys. J. **131**, 442 (1960).
[18] K. Burns, G. Vasil, J. Oishi, D. Lecoanet, and B. Brown, "Dedalus: Flexible framework for spectrally solving differential equations," Astrophysics Source Code Library (2016), ascl:1603.015.
[19] U. M. Ascher, S. J. Ruuth, and R. J. Spiteri, "Implicit-explicit Runge-Kutta methods for time-dependent partial differential equations," Applied Numerical Mathematics **25**, 151–167 (1997).
[20] David Goluskin, Hans Johnston, Glenn R. Flierl, and Edward A. Spiegel, "Convectively driven shear and decreased heatflux," J. Fluid Mech. **759**, 360–385 (2014).
[21] David Goluskin, *Internally Heated Convection and Rayleigh-Bénard Convection* (Springer International Publishing, 2016).
[22] F. Cattaneo, N. H. Brummell, J. Toomre, A. Malagoli, and N. E. Hurlburt, "Turbulent compressible convection," Astrophys. J. **370**, 282–294 (1991).

[23] L. Korre, N. Brummell, and P. Garaud, "Weakly non-Boussinesq convection in a gaseous spherical shell," Phys. Rev. E **96**, 033104 (2017), arXiv:1704.00817 [physics.flu-dyn].

[24] Guenter Ahlers, Siegfried Grossmann, and Detlef Lohse, "Heat transfer and large scale dynamics in turbulent rayleigh-bénard convection," Rev. Mod. Phys. **81**, 503–537 (2009).

[25] J. Otero, R. W. Wittenberg, R. A. Worthing, and C. R. Doering, "Bounds on Rayleigh Bénard convection with an imposed heat flux," J. Fluid Mech. **473**, 191–199 (2002).

[26] J. V. Wall and C. R. Jenkins, *Practical Statistics for Astronomers, by J. V. Wall , C. R. Jenkins, Cambridge, UK: Cambridge University Press, 2012* (2012).

[27] A. Brandenburg, "Stellar Mixing Length theory with entropy rain," arXiv (2016), arXiv:1504.03189.

[28] P. J. Käpylä, M. Rheinhardt, A. Brandenburg, R. Arlt, M. J. Käpylä, A. Lagg, N. Olspert, and J. Warnecke, "Extended Subadiabatic Layer in Simulations of Overshooting Convection," Astrophys. J. Lett. **845**, L23 (2017), arXiv:1703.06845 [astro-ph.SR].

[29] B. Paxton, L. Bildsten, A. Dotter, F. Herwig, P. Lesaffre, and F. Timmes, "Modules for Experiments in Stellar Astrophysics (MESA)," The Astrophysical Journal Supplement Series **192**, 3 (2011), arXiv:1009.1622 [astro-ph.SR].

[30] B. Paxton, M. Cantiello, P. Arras, L. Bildsten, E. F. Brown, A. Dotter, C. Mankovich, M. H. Montgomery, D. Stello, F. X. Timmes, and R. Townsend, "Modules for Experiments in Stellar Astrophysics (MESA): Planets, Oscillations, Rotation, and Massive Stars," The Astrophysical Journal Supplement Series **208**, 4 (2013), arXiv:1301.0319 [astro-ph.SR].

[31] B. Paxton, P. Marchant, J. Schwab, E. B. Bauer, L. Bildsten, M. Cantiello, L. Dessart, R. Farmer, H. Hu, N. Langer, R. H. D. Townsend, D. M. Townsley, and F. X. Timmes, "Modules for Experiments in Stellar Astrophysics (MESA): Binaries, Pulsations, and Explosions," The Astrophysical Journal Supplement Series **220**, 15 (2015), arXiv:1506.03146 [astro-ph.SR].

[32] B. Paxton, J. Schwab, E. B. Bauer, L. Bildsten, S. Blinnikov, P. Duffell, R. Farmer, J. A. Goldberg, P. Marchant, E. Sorokina, A. Thoul, R. H. D. Townsend, and F. X. Timmes, "Modules for Experiments in Stellar Astrophysics (MESA): Convective Boundaries, Element Diffusion, and Massive Star Explosions," The Astrophysical Journal Supplement Series **234**, 34 (2018), arXiv:1710.08424 [astro-ph.SR].

[33] W. D. Arnett, C. Meakin, M. Viallet, S. W. Campbell, J. C. Lattanzio, and M. Mocák, "Beyond Mixing-length Theory: A Step Toward 321D," Astrophys. J. **809**, 30 (2015), arXiv:1503.00342 [astro-ph.SR].

[34] A. Cristini, C. Meakin, R. Hirschi, D. Arnett, C. Georgy, and M. Viallet, "Linking 1D evolutionary to 3D hydrodynamical simulations of massive stars," Physica Scripta **91**, 034006 (2016), arXiv:1601.01572 [astro-ph.SR].